EPAPS

Leidenfrost vapor layers reduce drag without the crisis in high viscosity liquids

Ivan U. Vakarelski[1*], Joseph D. Berry[2, 3], Derek Y. C. Chan[4, 5], Sigurdur T. Thoroddsen[1]

[1] Division of Physical Sciences and Engineering & Clean Combustion Research Center, King Abdullah University of Science and Technology (KAUST), Thuwal 23955-6900, Saudi Arabia.

[2]Mineral Resources, Commonwealth Scientific & Industrial Research Organisation (CSIRO), Clayton VIC 3169, Australia

[3]Department of Chemical and Biomolecular Engineering, University of Melbourne, Parkville VIC 3010, Australia.

[4]School of Mathematics and Statistics, University of Melbourne, Parkville VIC 3010, Australia.

[5]Department of Chemistry and Biotechnology, Swinburne University of Technology, Hawthorn, VIC 3122, Australia.

[*]ivanuriev.vakarelski@kaust.edu.sa

1. Materials

The perfluorocarbon liquids used in the experiments were FLUTEC$^©$ High Performance fluids from F2 Chemicals Ltd: Flutec PP1, mostly composed of perfluoro-2-methylpentane (C_6F_{14}); Flutec PP3, of perfluoro-1,3-dimethylcyclohexane (C_8F_{16}); Flutec PP10, of perfluoroperhydrofluorene ($C_{13}F_{22}$) and Flutec PP11 of perfluoroperhydrophenanthrene ($C_{14}F_{24}$). These fluids are clear, colourless, fully-fluorinated liquids with large range of viscosities. Physical properties of the fluids, summarized in Table S1 are: density, ρ; boiling temperature, T_B; Leidenfrost temperature, T_L; dynamic viscosity of the liquid, μ_L; dynamic viscosity of the vapor, μ_V; vapor thermal conductivity, k_V; and surface tension, σ. Included in Table S1 are the properties of water at 95 ℃ and another perfluorocarbon liquid FC-72 (3M™ Fluorinert™ Electronic Liquid) used in earlier work.

The FLUTECH fluids viscosities were precisely measured using Ubbelohde type capillary viscometer (Fungilab). We noticed that the PP11 viscosity of about 19.0 mPa s measured by us differ from the producer given value of 28.4 mPa s (http://www.f2chemicals.com/). However, we confirmed the PP11viscosity value of about 19.0 ± 0.2 mPa s using a rotational viscometer (Hakke 6 plus, Thermo Scientific), and by measuring the terminal velocity of glass microsphere of Re < 0.1.

The spheres used in the free fall experiments were polished grinding balls (FRITSCH GmbH) of various materials: sintered corundum (ρ_s = 3.8 g/cm^3, $2R$ = 10, 15, 20 mm); stainless steel (ρ_s = 7.7 g/cm^3, $2R$ = 10, 15, 20 mm); tungsten carbide (ρ_s = 14.9 g/cm^3, $2R$ = 10, 15 mm). The average surface roughness given by the manufacturer is R_a < 0.06 μm. The sphere were rinsed with ethanol and water and dried before use.

2.   Sphere cooling rate and vapor layer thickness estimation

High-speed video snapshots of a heated steel sphere held stationary in fluorinated liquid are shown in Fig. S1. When the sphere temperature is above the Leidenfrost temperature, $T_S > T_L$, the sphere is encapsulated in a continuous vapor layer (Fig. S1a), as is evident by the ripple waves driven by buoyancy moving along the sphere surface and the periodic pinch off bubbles separating from the top of the sphere. When the sphere cools below the Leidenfrost temperature, $T_S < T_L$, the rupture of the vapor layer is marked by an intensive release of bubbles through nucleate boiling (Fig. S1b). Videos of this sphere cooling process in FC-72 liquid and in 95 ºC water are available in ref. [S1] and [S2], respectively. Visual observation and high-speed camera recording of the spheres cooling process in various Flutec liquids confirmed that the cooling process occurs in a similar way to that in FC-72 fluid with the only major difference being in the value of the Leidenfrost temperature as indicated below.
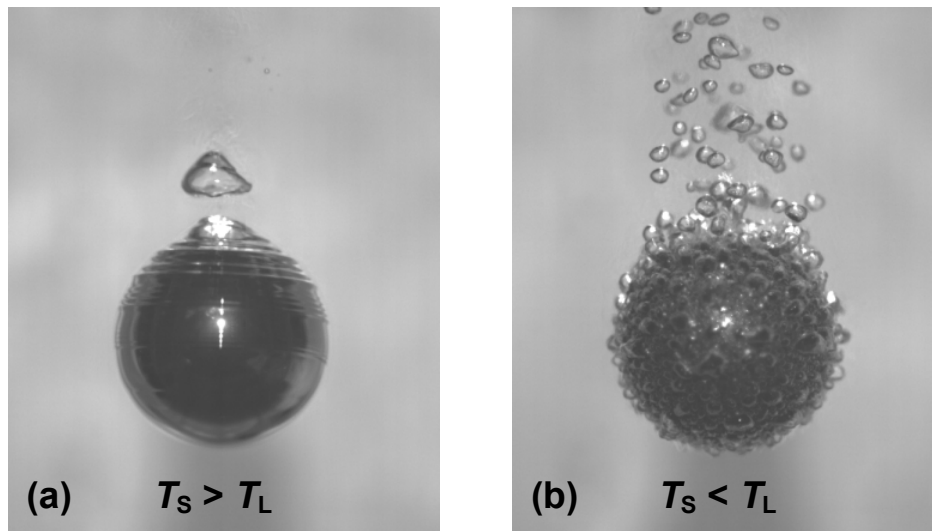
Supplemental Figure S1. High-speed camera snapshots of a 15 mm steel sphere held stationary in FC-72 fluorocarbon liquid, (a) when the sphere temperature, T_S is above the Leidenfrost temperature, T_L and (b) shortly after cooling below T_L. See also ref. [S1] that contains video of the process in the case of FC-72 liquid and ref. [S3] for the case of water.

The sphere temperature vs. time variation for a 30 mm steel sphere cooling in PP1 (blue); PP2 (green); PP10 (brown) and PP11 (red) is shown in Fig. S2a. The temperature of the stationary sphere was monitored using a thermocouple probe inserted into the centre of the sphere. The abrupt change in the slope of the temperature curves indicates the Leidenfrost transition point characterized by the Leidenfrost temperatures, T_L for each liquid (see Table S1). Further details for this type of measurement can be found in references [S2] and [S3]. The Leidenfrost temperatures given in Table S1 are measured on stationary spheres. However a higher sphere temperature might be needed to maintain a stable vapor layer on a sphere that is free falling in the fluid [S2]. To secure the stability of the Leidenfrost regimen on the falling spheres, before release the spheres were heated to T_S = 220 ℃ in PP1, T_S = 300 ℃ in PP3, T_S = 400 ℃ in PP10, and T_S = 450 ℃ in PP11.

The cooling rate dT_S/dt can be used to estimate the average thickness, λ_V of the vapor layer surrounding the sphere during cooling in the Leidenfrost regime, using the following relations [S3, S4]:

$$\lambda_V = \left(\frac{3k_v}{\rho c_p R} \right) \frac{(T_S - T_{sat})}{(dT_S / dt)} \qquad\qquad \text{S1}$$

where ρ = 7,700 kg m^{-3} is the density of the steel sphere, c_p = 466 J kg^{-1} K^{-1} is the steel sphere specific heat, k_v is the vapor thermal conductivity, T_S is the sphere temperature, T_{sat} is the saturation temperature of the liquid, and dT_S/dt is the sphere cooling rate estimated from the cooling curves in Leidenfrost regime (Fig S2a). We notice that the vapor thermal conductivity k_v, varies with the vapor temperature, as well as between the components used. The estimates of the vapor thicknesses given in Fig. S2b were made using the values, k_v provided by the manufacturer at vapor temperature of about 240 ℃ (Table S1). The value of k_v for PP11, was not available and is approximated instead with the PP10 value.

From our sphere cooling experiments we estimated the characteristic thickness of the vapor layer on a static sphere to be of about 150 ± 50 μm (Fig S2b). This estimate range is very close to prior estimates using direct observation of the vapor layer on the sphere [S1].

a

b
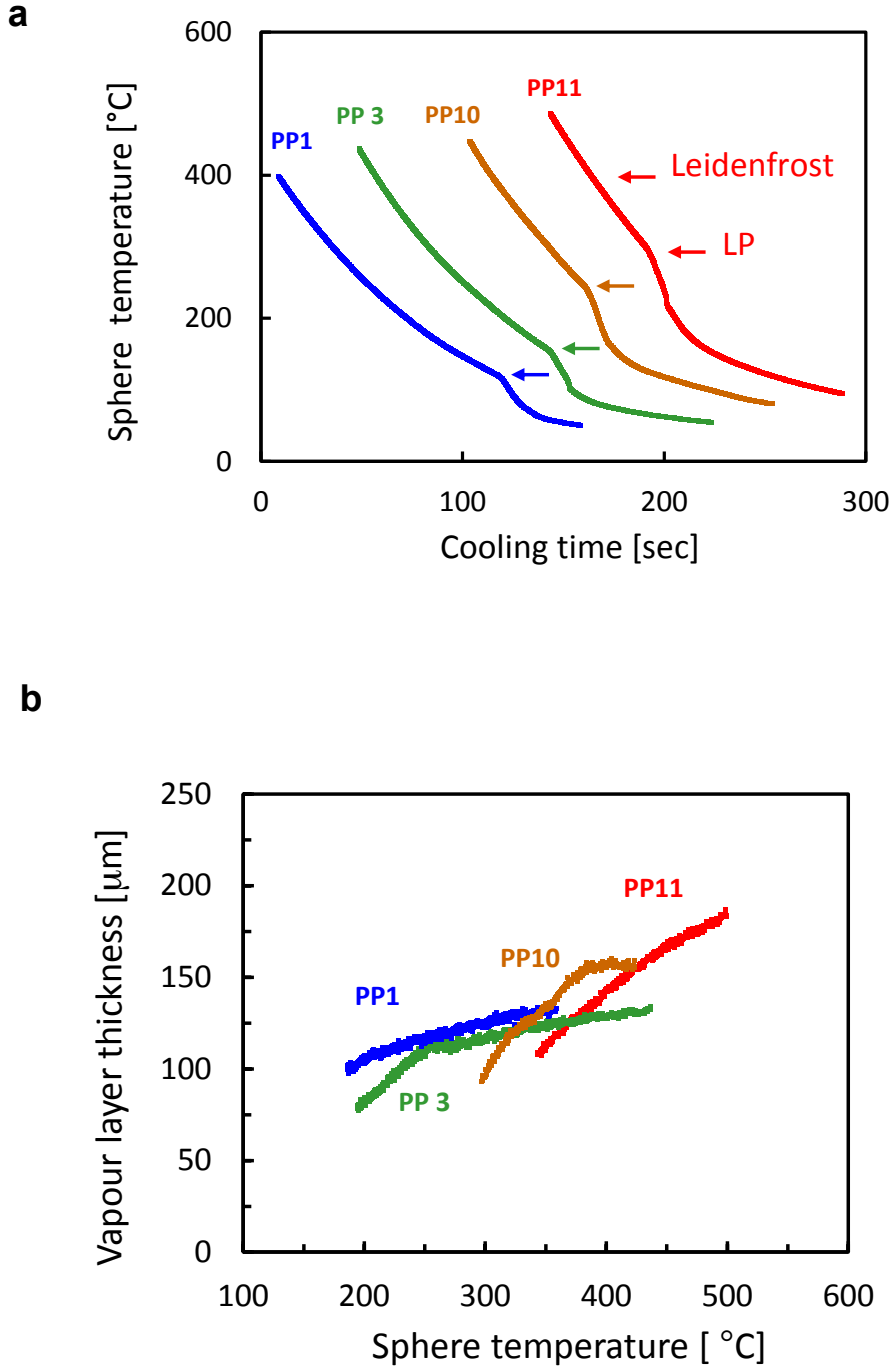
Supplemental Figure S2. (a) Sphere temperature *vs* cooling time for a stationary 30 mm diameter steel sphere cooling in Flutec PP1 (blue), PP3 (green), PP10 (brown) and PP11 (red). Arrows mark the Leidenfrost point at temperature T_L. (b) Vapor layer thickness on a static sphere estimated using equation S1, with dT_S/dt calculated from data in (a) for each liquid and k_v values at 240 ℃ (Table S1).

3.   Free falling sphere experiments

The sphere free fall in liquid experiment used to determine their terminal velocity and drag coefficient follow the experimental protocol detailed in our earlier studies [S1] and [S2] and specific details are given below.

The liquid tank in which the sphere fall experiments were conducted was 1.6 meter tall and has a cross section of 10 cm × 10 cm. The tank is made of clear Acrylic with a wall thickness of 8 mm. Spheres were heated to the desired temperature in a temperature control furnace for at least 30 minutes. The heated spheres were held by metal forceps and carefully released from below the liquid surface at the top of the tank.

The sphere fall was monitored by a high-speed video camera (Photron Fastcam SA-5) with a typical filming frame rate of 1000 fps. The sphere location *vs* time and the corresponding instantaneous velocity was determined by image processing the videos with the camera software (Photron FASTCAM Viewer, PFV Ver.3262). Figure S3 shows an example for the sphere velocity progression toward the bottom of the tank for PP3 fluid and 20 mm steel sphere held at room temperature, $T_S = 21$ ^{0}C, or held in the Leidenfrost regime, $T_S = 350$ ^{0}C. For all spheres and fluids studied, the room temperature spheres were able to reach terminal velocity before the bottom of the tank. For the largest spheres falling in Leidenfrost regime (2R = 20 mm, steel and tungsten carbide spheres) at the end of the fall the sphere might still be accelerating, in which case the velocity close to the bottom of the tank was used to make an upper bound estimate for the drag coefficient [S2]. The drag coefficient C_D, was determined from the terminal velocity U_T of the sphere of diameter 2R using the relation:

$$C_D = (8[\rho_s - \rho]gR)/(3\rho U_T^2) \hspace{4cm} S2$$

where, g is the gravitational acceleration, ρ the liquid density and ρ_s the sphere density. The terminal velocity was corrected for the effect of the tank walls using the following correction formula due to Newton (1687):

$$U_T/U_{T\infty} = [1 - (D/D_c)^2] [1 - 0.5(D/D_c)^2]^{1/2} \hspace{3cm} S3$$

6

where U_T is the measured terminal velocity, $U_{T\infty}$ is the corrected terminal velocity for an infinite flow domain, D is the sphere diameter and D_c is the diameter of a cylindrical tank. For the $a \times a$ square cross-section tank used in the present experiment, the effective diameter D in eq. S3 is calculated by equating the areas of the circle and the square, i. e. $D_c = \left(2/\sqrt{\pi}\right)a$.
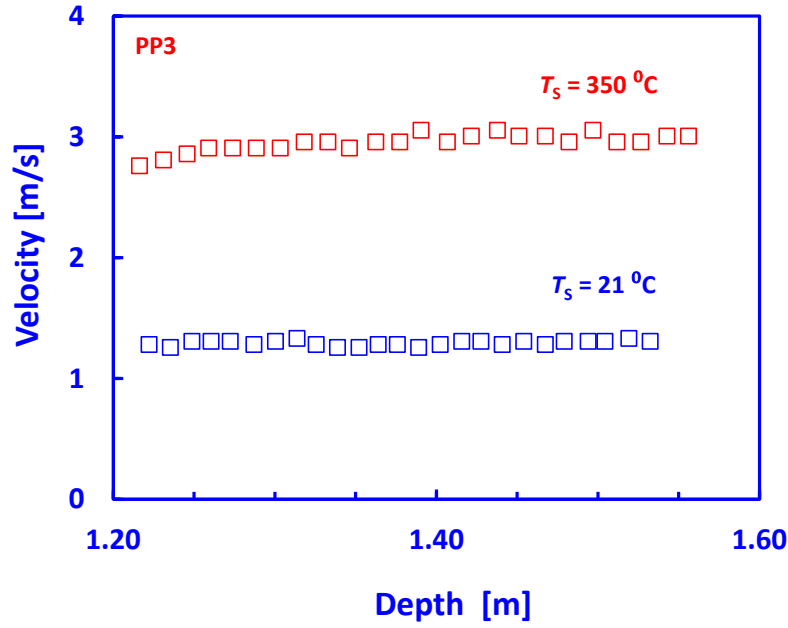

Supplemental Figure S3. Velocity vs. depth data for free fall of 20 mm steel sphere in PP3 approaching the bottom of the 1.6 m tank for the case of room temperature sphere, $T_S = 21\ ^0C$ (open squares, blue) and Leidenfrost regime sphere , $T_S = 350\ ^0C$ (open squares, red).

Figure S4 is a collection of C_D vs. Re data obtained for the four Flutec fluids studied: PP1 (Fig. S4a); PP3 (Fig. S3b); PP10 (Fig. S4c) and PP11 (Fig. S4d). The PP3 and PP11 data are also presented in the manuscript Fig. 1. In each case the drag of the room temperature spheres for the no vapor case is compared with the drag on sphere falling in Leidenfrost regime.

a

b
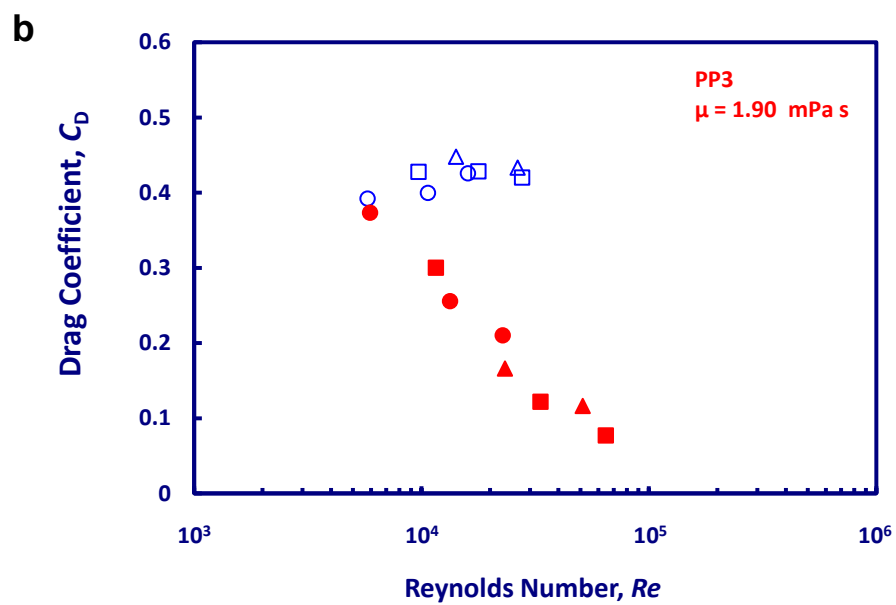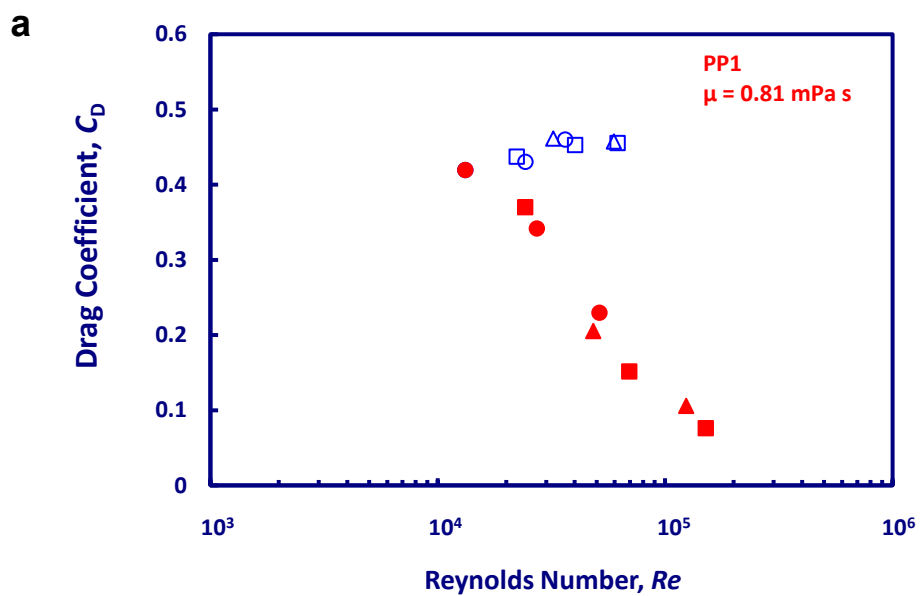
Supplemental Figure S4a, S4b. (see next page for the captions)

c

d
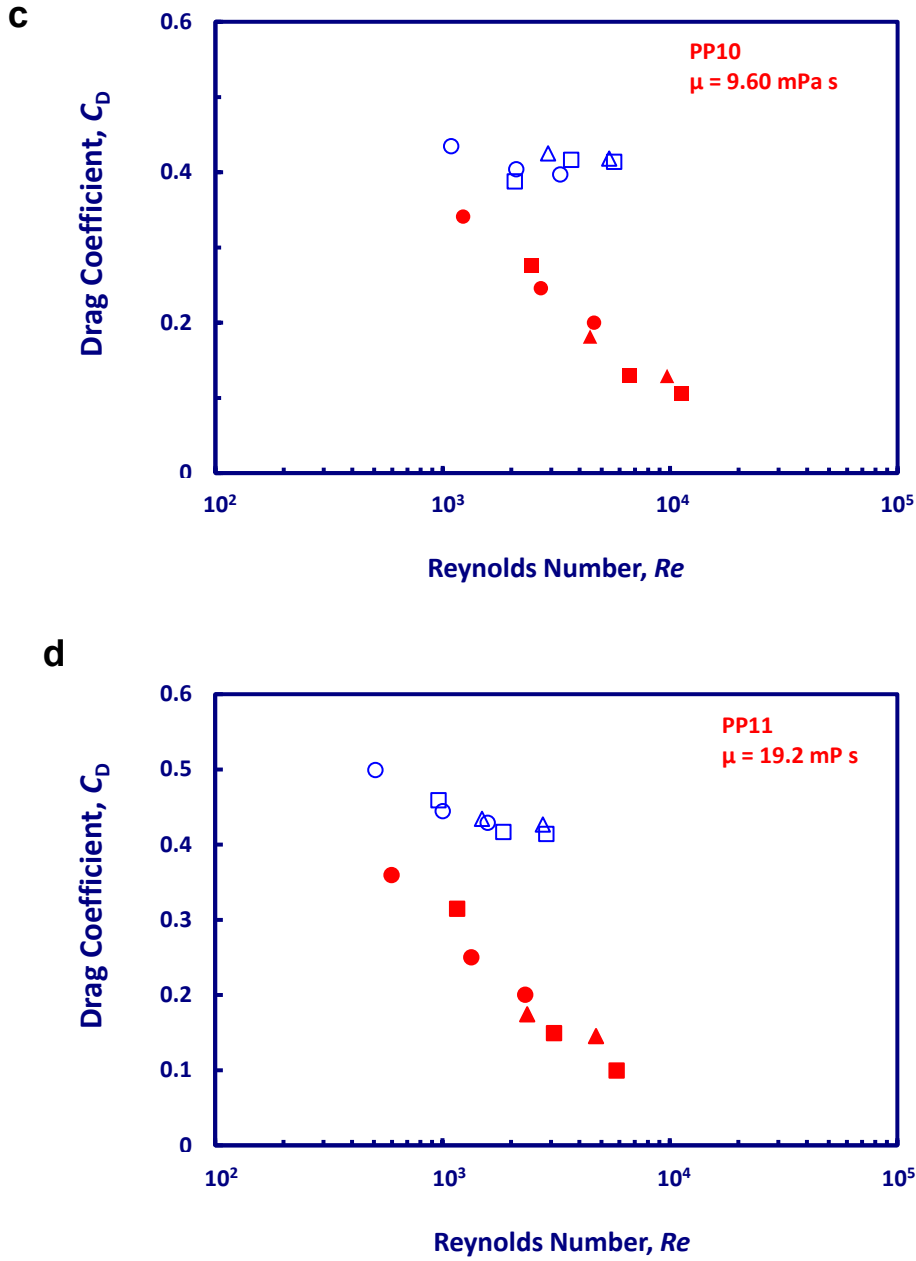
Supplemental Figure S4. Dependence of the drag coefficient, C_D on the Reynolds number, Re for spheres free falling in the Leidenfrost regime (solid symbols) at various initial sphere temperatures, T_S (a) PP1: $T_S = 220$ ℃; (b) PP3: $T_S = 300$ ℃; (c) PP10: $T_S = 400$ ℃; (d) PP11: $T_S = 450$ ℃. Open symbols are for spheres at room temperature. Symbol shapes denote different materials: steel (square, $2R = 10$; 15; 20 mm), sintered corundum (circles, $2R = 10$; 15; 20 mm) and tungsten carbide (triangles, $2R = 10$; 15).

4.   Numerical simulations

Direct numerical and large eddy simulations (DNS and LES respectively) were performed using ANSYS Fluent 15.0 on a rectangular domain extending 16D upstream and 21D downstream of the sphere centre, and 16D in the directions normal to the flow (here D is the sphere diameter). The sphere diameter was set to a nominal diameter of 1 m, and the fluid was nominally chosen as air of density $\rho = 1.225$ kg/m³ and viscosity $\mu = 1.7894 \times 10^{-5}$ Pa.s. The normal velocity at the upstream boundary was specified as a constant velocity U, chosen to give the desired Reynolds number. The corresponding tangential velocities were set to zero. The tangential velocity in the flow direction on the four boundaries normal to the flow were also specified as U, with the other two velocity components set to zero. The downstream boundary was specified as an outlet, with zero normal velocity gradient.

Two types of boundary conditions were considered on the sphere surface. To model flow past a no-slip sphere, zero velocity was imposed at the sphere surface. For partial-slip spheres, a user-defined function was written to implement the Navier slip boundary condition on the sphere surface, defined as [S5]:

$$\boldsymbol{t}^{(i)} \cdot \boldsymbol{u} = \frac{1}{2}\frac{\lambda_S}{R}\boldsymbol{t}^{(i)}\boldsymbol{n}\!:\!\boldsymbol{\tau}$$

S4

Here λ_S/R is the dimensionless slip length; $\boldsymbol{t}^{(i)}$ and $\boldsymbol{n}$ are the unit vectors tangential and normal to the surface respectively; $\boldsymbol{u}$ is the fluid velocity; and $\boldsymbol{\tau}$ is the fluid shear stress. The implementation of the Navier slip boundary condition was validated at Re $\ll$ 1 against the Stokes flow analytical solution for a free slip bubble [S6].

The first mesh point normal to the sphere surface was located within one dimensionless viscous unit, $r^+ = 1$, with r^+ defined as:

$$\Delta r^+ = \frac{\rho U_\tau r}{\mu}$$

S5

Here r is the distance from the wall, $u_\tau = \sqrt{\tau_{w.}/\rho}$ is the (maximum) friction velocity, and τ_w is the (maximum) surface shear stress. The friction velocity was estimated as $0.04U$ *a*

10

priori, consistent with the approach of Constantinescu & Squires [S8], and then checked for validity *a posteriori*. The growth rate in mesh size close to the wall was specified as 1.06, with at least 7 mesh points within 10 wall units of the sphere. The maximum size of elements on the sphere surface was approximately 5 – 36 wall units, depending upon the size of Reynolds number chosen (Table S2). Away from the sphere, the growth rate in mesh size in the upstream and flow normal directions was specified as 1.12, whilst the growth rate in the wake region was specified as 1.02. The mesh size was approximately 6.26 million elements for the lower Re simulations, and 12.6 million elements for the higher Re simulations (Table S2).

Simulations were run using SIMPLE pressure-velocity coupling and second-order implicit time stepping. DNS simulations were run with second-order upwind spatial discretisation, whereas LES simulations used bounded central difference spatial discretisation. The time step was set to $\Delta t = 0.02\, D/U$, ensuring adequate resolution of shedding frequencies. At each time step the convergence criterion was set to 10^{-4} for the non-dimensional velocity and pressure residuals. For Re > 10^4, LES was used to model the effects of turbulence.

Reynolds number	Method	No. of elements within the first viscous unit (normal to sphere)	Maximum size of elements on sphere in viscous units	Total number of elements
2.3×10^3	DNS	13.4	5.0	$\sim6.26\times10^6$
5.8×10^3	DNS	6.7	9.9	$\sim6.26\times10^6$
2.3×10^4	LES	1.5	27.9	$\sim6.26\times10^6$
6.0×10^4	LES	1.2	36.7	$\sim12.6\times10^6$

Table S2: Properties of the meshes used for simulations. The viscous unit is defined in Equation S4.

Consistent with previous studies, the dynamic Smagorinsky model (DSM) was used [S7-S14]. In this model, the sub-grid scale stresses τ_{ij} are modeled using the Boussinesq hypothesis as

$$\tau_{ij} - \frac{1}{3}\delta_{ij}\tau_{kk} = -\mu_t \bar{S}_{ij}. \qquad\qquad\qquad S6$$

Here $\bar{S}_{ij}$ is the resolved rate-of-strain tensor, and μ_t is the eddy viscosity. In the standard Smagorinsky model, the eddy viscosity is defined as:

$$\mu_t = (C_S\Delta)^2 \rho \sqrt{2\bar{S}_{ij}\bar{S}_{ij}}, \qquad\qquad\qquad S7$$

here Δ is the filter width, and C_S is the Smagorinsky constant, usually set to 0.1. However, setting C_S as constant does not necessarily yield accurate results. In DSM, the Smagorinsky constant is adjusted in space and time dependent upon the energy content of the smallest scale eddies resolved in the flow field [S9, S10].

The sub-grid scale stress model assumption inherent in LES may give rise to errors in laminar flow regions, which may slightly delay the boundary layer separation, and therefore modifying the drag-reduction mechanism. To confirm that this potential source of error is negligible in our simulations, in Figure S5 we compare our DNS and LES results to previous experimental and numerical observations available in the literature [S8, S11-13, S15-20]. Our results compare extremely well with previous experimental and numerical observations, and there is no discernable difference in trend when comparing our DNS results to our LES results. In conclusion, we see no evidence of an artificial delay in boundary-layer separation introduced by LES in the subcritical Reynolds number range that we consider here.
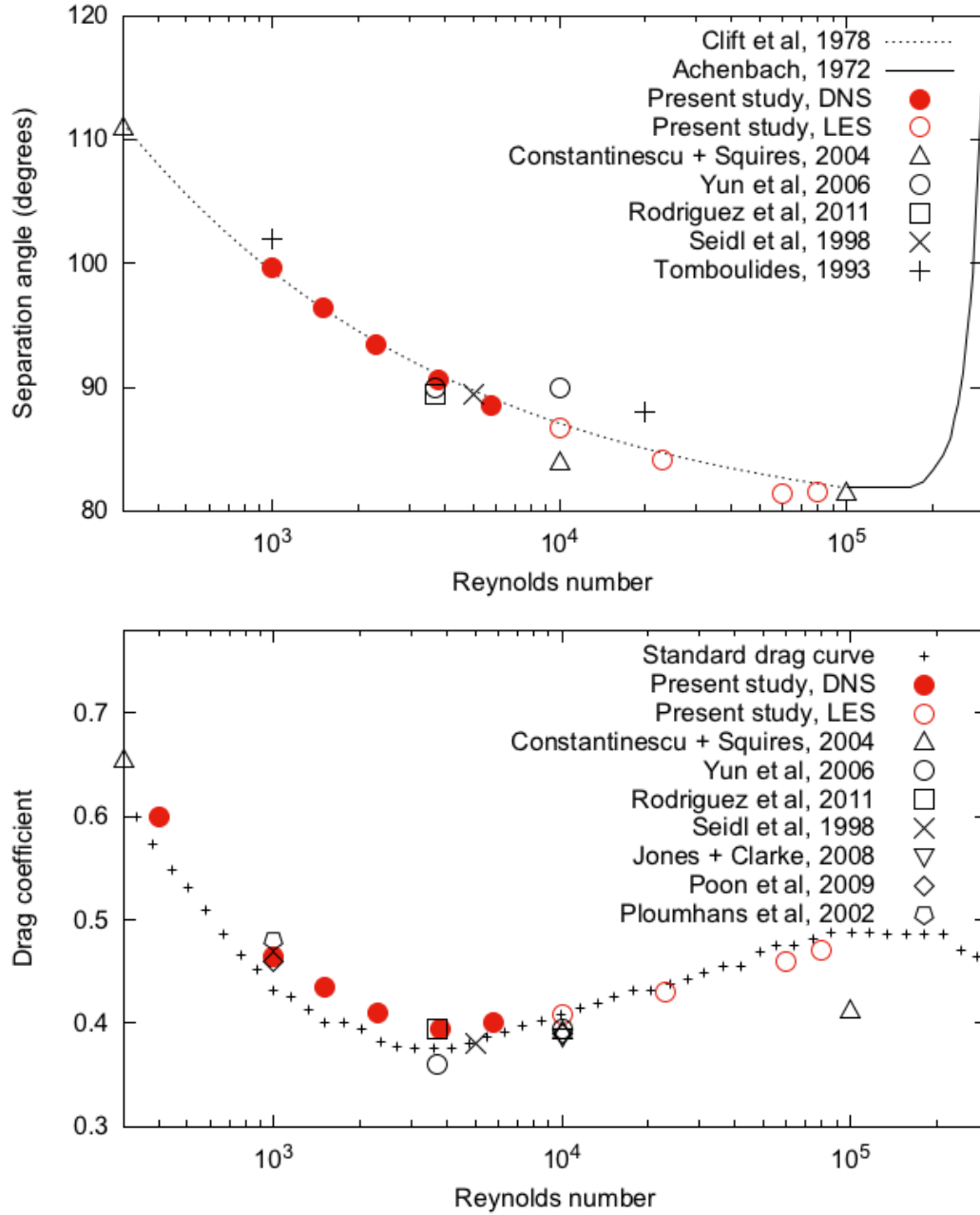
Supplemental Figure S5. Comparison of DNS and LES predictions of separation angle and drag coefficient to experimental and numerical data in the literature over a wide range of subcritical Reynolds numbers.

References

S1. I. U. Vakarelski, J. O. Marston, D. Y. C. Chan, and S. T. Thoroddsen, Phys. Rev. Lett. **106**, 214501 (2011).

S2. I. U. Vakarelski, D. Y. C. Chan, and S. T. Thoroddsen, Soft Matter **10**, 5662 (2014).

S3. I. U. Vakarelski, N. A. Patankar, J. O. Marston, D. Y. C. Chan, and S. T. Thoroddsen, Nature **489**, 274-277 (2012).

S4. H. I. Jouhara, and B. P. Axcell, Trans. I Chem E, Part A (Chem. Eng. Res. Design) **80**, 284-289 (2002).

S5. J. W. Swan and A. S. Khair, J. Fluid Mech. **606**, 115 (2008).

S6. H. Lamb, Hydrodynamics (Dover Publications, New York, 1932)

S7. G. S. Constantinescu and K. D. Squires, Flow Turbul. Combust. **70**, 267 (2003).

S8. G. Constantinescu and K. Squires, Phys. Fluids **16**, 1449 (2004).

S9. M. Germano, U. Piomelli, P. Moin, and W. H. Cabot, Phys. Fluids A **3**, 1760 (1991).

S10. D. K. Lilly, Phys. Fluids, **4**, 633 (1992).

S11. D.A. Jones and D.B. Clarke, Defence Science and Technology Organisation internal report, DSTO-TR-2232 (2008).

S12. G. Yun, D. Kim and H. Choi, Phys. Fluids **18**, 015102 (2006).

S13. E. K. W. Poon, G. Iaccarino, A.S.H. Ooi and M. Giacobello, in Proc. 7th Int. Conf. of CFD in the Minerals and Process Industries (2009).

S14. S. Jindal, L. Long, P. Plassmann and N. Uzol, in Proc. 34th AIAA Fluid Dynamics Conf. 2228 (2004).

S15. R. Clift, J. Grace, and M. Weber, Bubbles, drops, and particles (Academic Press, New York, 1978).

S16. E. Achenbach, J. Fluid Mech. **54**, 565 (1972).

S17. I. Rodriguez, R. Borell, O. Lehmkuhl, C. D. Perez Segarra, and A. Oliva, J. Fluid Mech. **679,** 263 (2011).

S18. V. Seidl, S. Muzaferija, and M. Perić, Appl. Sci. Res. 59, 379 (1997).

S19. A. G. Tomboulides, PhD thesis, Princeton University (1993).

S20. P. Ploumhans, G. S. Winckelmans, J. K. Salmon, A. Leonard and M. S. Warren, J. Comp. Phys **178,** 427 (2002).

Supplemental Video Legends:

Video 1. Combined video comparing the fall of a 20 mm steel sphere in Flutec PP3 fluids at T_S = 21 °C (left side, no vapor case), T_S = 175 °C (middle, nucleate boiling case) and T_S = 300 °C (right side, the Leidenfrost regime). The frame rate used was 2000 fps and the video playback speed is 30 fps.

Video 2. Combined video showing the fall of a 20 mm steel sphere in Flutec PP11 fluids at T_S = 21 °C (left side, no vapor case), T_S = 350 °C (middle, nucleate boiling case) and T_S = 450 °C (right side, Leidenfrost regime). The frame rate used was 1000 fps and the video playback speed is 30 fps.

Video 3. Animated comparison of the experimental wake visualisation for a 20 mm sphere falling in PP3 fluid with the large eddy simulation results. The top panels show the no-slip comparisons for the nucleate boiling case of T_S = 175 ^{0}C with the simulation parameters λ_S/R = 0, Re = 2.3 x10^4, and the bottom panels show the partial slip comparison for the Leidenfrost case of T_S = 300 ^{0}C with the simulation parameters λ_S/R = 0.012 and Re = 6×10^4. Shown are the experimental wake visualisations (left) using Video 1 clips, numerical wake visualisation (middle), and numerical instantaneous out-of-plane vorticity contours (right). The wake was visualised numerically by solving an advection-diffusion equation for the transport of a scalar species within the flow domain, with a Dirichlet boundary condition at the sphere surface. The diffusivity of the scalar species was set equal to the diffusivity of the surrounding fluid.

Liquid	Chemical formula	Density ρ [10^3 kg/m³]	Boiling temperature T_B [°C]	Leidefrost temperature[a] T_L [°C]	Liquid dynamic viscosity μ_L [mPa s]	Vapor dynamic viscosity[b] μ_v [10^{-2} mPa s]	Liquid thermal conductivity[c] k_v [W/K]	Surface tension σ [mN/m]
FC 72	C_6F_{14}	1.68	56	116	0.64	1.10	n/a	10.0
PP1	C_6F_{14}	1.71	57	116	0.81 [d]	1.16	27	11.9
PP3	C_8F_{16}	1.83	102	140	1.90 [d]	1.25	36	16.6
PP10	$C_{13}F_{22}$	1.98	194	230	9.60 [d]	n/a	53	19.7
PP11	$C_{14}F_{24}$	2.03	215	290	19.20 [d]	n/a	n/a	19.0
Water at 95 ºC	H_2O	0.96	100	235	0.30	1.2	36	61.0

Table S1: Physical properties of the liquid used: density, ρ; boiling temperature, T_B; Leidenfrost temperature, T_L; dynamic viscosity of the liquid, μ_L; dynamic viscosity of the vapor, μ_L; vapor thermal conductivity, k_v; and surface tension, σ.

Notes

[a] as measured on a static 30 mm steel sphere cooling in the liquid (Fig. S2a).

[c] μ_v values at boiling point of the fluid. PP1and PP3 values provided by F2 Chemicals.

[c] k_v at about 240 ºC. PP1; PP3 and PP10 values provided by F2 Chemicals.

[d] measured at 21 ºC by Ubbelohde capillary viscometer